

Journal of Materials Chemistry A

Materials for energy and sustainability

Accepted Manuscript

This article can be cited before page numbers have been issued, to do this please use: Z. Shen, Y. Zhuang, W. Li, X. Huang, F. E. Oropeza, E. J.M. Hensen, J. P. Hofmann, M. Cui, A. Tadich, D. Qi, J. Cheng, J. Li and K. H. L. Zhang, *J. Mater. Chem. A*, 2020, DOI: 10.1039/C9TA13313E.



This is an Accepted Manuscript, which has been through the Royal Society of Chemistry peer review process and has been accepted for publication.

Accepted Manuscripts are published online shortly after acceptance, before technical editing, formatting and proof reading. Using this free service, authors can make their results available to the community, in citable form, before we publish the edited article. We will replace this Accepted Manuscript with the edited and formatted Advance Article as soon as it is available.

You can find more information about Accepted Manuscripts in the [Information for Authors](#).

Please note that technical editing may introduce minor changes to the text and/or graphics, which may alter content. The journal's standard [Terms & Conditions](#) and the [Ethical guidelines](#) still apply. In no event shall the Royal Society of Chemistry be held responsible for any errors or omissions in this Accepted Manuscript or any consequences arising from the use of any information it contains.

Increased Activity in the Oxygen Evolution Reaction by Fe⁴⁺-Induced Hole States in Perovskite La_{1-x}Sr_xFeO₃

Zechao Shen^a, Yongbin Zhuang^a, Weiwei Li^b, Xiaochun Huang^a, Freddy E. Oropeza^c, Emiel J. M. Hensen^c, Jan P. Hofmann^c, Meiyuan Cui^a, Anton Tadich^{d,e}, Dongchen Qi^f, Jun Cheng^a, Jun Li^{a*}, Kelvin H. L. Zhang^{a*}

*Corresponding authors

^a State Key Laboratory of Physical Chemistry of Solid Surfaces, College of Chemistry and Chemical Engineering, Xiamen University, Xiamen 361005, P.R. China

^b Department of Materials Science & Metallurgy, University of Cambridge, 27 Charles Babbage Road, Cambridge, CB3 0FS, United Kingdom

^c Laboratory for Inorganic Materials and Catalysis, Department of Chemical Engineering and Chemistry, Eindhoven University of Technology, P. O. Box 513, 5600 MB Eindhoven, The Netherlands

^d Australian Synchrotron, 800 Blackburn Road, Clayton, Victoria 3168, Australia

^e Department of Chemistry and Physics, La Trobe University, Melbourne, Victoria 3086, Australia

^f School of Chemistry, Physics and Mechanical Engineering, Queensland University of Technology, Brisbane, Queensland 4001, Australia

Email: junnyxm@xmu.edu.cn; kelvinzhang@xmu.edu.cn

Abstract

Perovskite transition metal oxides are promising non-precious metal electrocatalysts for promoting the oxygen evolution reaction (OER) in many electrochemical energy conversion devices. This work reports a systematic study of the relation between the electronic structure and OER performance of perovskite La_{1-x}Sr_xFeO₃ ($0 \leq x \leq 1$). The partial substitution of La for Sr in LaFeO₃ results in the oxidation of Fe³⁺ to Fe⁴⁺ and substantially enhances OER activity. A comprehensive X-ray spectroscopic study reveals a strong correlation of the enhanced OER activity with these Fe⁴⁺ states. The presence of Fe⁴⁺ leads to a stronger Fe-O bond due to stronger Fe 3d-O 2p orbital hybridization and shifts the energy position of the valence band (VB) to E_F. Such an electronic modulation optimizes the surface adsorption energetics of *OH intermediates, contributing to faster OER kinetics. Furthermore, a new unoccupied state is created at ~0.9 eV below the conduction band. This hole state reduces the energy barrier for electron transfer from 1.34 eV to 0.44 eV, thereby facilitating charge transfer at the interface. The Fe⁴⁺-induced electronic states responsible for higher OER activity have implications for the understanding of structure-activity relationships in other Fe-based electrocatalysts such as the highly active Fe-doped NiOOH.

Keywords: Perovskite; Electronic structure; Electrocatalyst; Structure-activity relationship; Transition metal oxides; Oxygen evolution reaction;

Introduction

Electrolysis of water to produce hydrogen and oxygen is a promising pathway for storage of intermittent renewable energy in form of chemical fuels.¹ Water splitting can be divided into two half reactions, the hydrogen evolution reaction (HER, $4\text{H}_2\text{O} + 4\text{e}^- \rightarrow 2\text{H}_2 + 4\text{OH}^-$) and the oxygen evolution reaction (OER, $4\text{OH}^- \rightarrow \text{O}_2 + 2\text{H}_2\text{O} + 4\text{e}^-$). The OER involves a thermodynamically uphill and complex four-electron/proton transfer process, and is usually the bottleneck limiting the overall efficiency of water splitting.^{2, 3} Hence, the development of abundant, stable and efficient OER electrocatalysts is the key for large-scale hydrogen production from renewable energy.

In recent years, perovskite transition metal oxides have been intensively explored as active electrocatalysts.⁴ Perovskite structure has a general formula of ABO_3 , with rare-earth and alkaline cations at the A site and earth abundant transition-metal cations (TM = Fe, Co and Ni) at the B site. Their properties can be substantially modified by substitution of the rare-earth for alkaline cations at A site, *e.g.*, La^{3+} for Sr^{2+} . This is because such substitution pushes the B site TM cation to a higher oxidation state, inducing a significant change in the electronic properties. Electronic structure parameters such as density of state (DOS) near the Fermi level (E_F) dictate the binding strength with reaction intermediates, and hence the activation barrier for the rate determining step (RDS) for OER.⁵ Following these concepts, a number of descriptors based on the material properties of perovskites have been correlated with the OER activity. For example, an early work in 1980s by Matsumoto *et al.* suggested that the OER activity of perovskite oxides increases with the bandwidth of the unoccupied σ^* band, because an extended σ^* band accelerates the electron transfer between the *OH and the catalyst surface.⁶ Bockris and Otagawa claimed that the OER activity would increase as the TM–OH bond strength decreases; while at the same time the increase in the number of *d*-electrons of the perovskite TM cations would weaken the TM–OH bond strength, thereby increasing the OER activity.⁷ However, this is opposite to the decrease in the number of *d* electrons on the Co cation upon Sr-doping of LaCoO_3 , which also increases the OER activity.⁸ Suntivich *et al.* proposed a volcano type correlation between the OER activity and the occupancy of the e_g orbital of TM cations.⁹ They found that perovskites with e_g occupancy of one electron (*e.g.*, LaNiO_3 and $\text{La}_{1-x}\text{Sr}_x\text{CoO}_3$) have the highest activities, whereas a high e_g filling results in too weak

binding of *OH intermediates and a low e_g filling in too strong binding. Other descriptors such as the position of the O 2p band center relative to the E_F,¹⁰ transition metal 3d-O 2p covalency,¹¹ and the participation of lattice oxygen have also been proposed.¹² This knowledge provides essential guidelines to design highly active electrocatalysts by tailoring these electronic parameters through doping,^{13, 14} strain¹⁵⁻¹⁷ and creation of oxygen defects.¹⁸ In this context, cobalt-containing perovskite oxides are the most extensively explored materials, in which the electronic structures can be tuned by substitution of Sr²⁺ for La³⁺, *e.g.*, La_{1-x}Sr_xCoO₃.¹⁹

LaFeO₃ (LFO) is a p-type semiconductor with a bandgap of ~ 2.2 eV.²⁰ Furthermore, Fe is the most abundant, low-cost and environmentally benign metal. LFO has been widely used in many applications such as photoelectrochemical water splitting, batteries, sensors, and solid oxide fuel cells.²¹⁻²⁴ Although stoichiometric LFO displays a poor OER and oxygen reduction reaction (ORR) performance, a recent report has demonstrated that A-site deficiency (La_{0.95}FeO_{3-δ}) significantly enhanced both OER and ORR performance in an alkaline solution.²⁵ More earlier, Wattiaux and co-workers studied the electrocatalytic activities of La_{1-x}Sr_xFeO_{3-y}.²⁶ Recently, She *et al.* reported that Sr doping in LFO increases OER activity.²⁷ The authors attributed the enhanced activity to surface oxygen vacancies and Sr doping induced change of electronic structures. However, there is a lack of understanding of how Sr doping influences the electronic structure and its relationship with OER activity. Fe cations in LFO have a nominal oxidation state of +3 ($t_{2g}^3e_g^2$). La³⁺ substitution with Sr²⁺ results in an increase in the nominal Fe oxidation state from +3 to +4 ($t_{2g}^3e_g^1$). Therefore, Sr doping in LFO offers a systematic approach to study the relationships of composition, electronic structure and OER performance beyond Co-based perovskites. Such insight is of paramount importance for the rational design of highly active, earth abundant electrocatalysts.

In this work, we performed a detailed study on the influence of Sr doping on the electronic structure of La_{1-x}Sr_xFeO₃ (LSFO-x) and the resulting OER activity. LSFO samples with Sr contents of x = 0, 0.1, 0.33, 0.67, 0.8 and 1 were synthesized by a

modified Pechini sol-gel method.²⁸ The evolution of electronic structure with Sr doping was investigated by X-ray photoemission spectroscopy (XPS), X-ray absorption spectroscopy (XAS) and DFT+U calculations. The OER activity was considerably enhanced with increasing Sr contents and LSFO-0.8 was identified as the most active catalyst. The enhanced activity was rationalized in terms of two key electronic structure modulations brought about by the presence of Fe⁴⁺ favoring OER: (i) the shift of the valence band (VB) center with enhanced Fe 3d-O 2p hybridization to E_F helps to stabilize the surface adsorption of *OH intermediate and (ii) the creation of a new unoccupied hole state reduces the energy barrier for electron transfer, and therefore promotes a faster kinetics for OER.

RESULTS AND DISCUSSION

Synthesis and characterization

Perovskite LSFO-x ($x = 0, 0.1, 0.33, 0.67, 0.8$ and 1) polycrystalline powders were synthesized by a modified Pechini sol-gel method.²⁸ The ratio of La to Sr was confirmed by inductively coupled plasma optical emission spectroscopy (ICP-OES), being very close to the intended doping values (see Table S1). Fig. 1a shows the Rietveld refined X-ray diffraction (XRD) patterns for LFO, LSFO-0.33, LSFO-0.67, LSFO-0.8 and SFO (see Fig. S1 for others). XRD patterns of LFO and LSFO-0.33 are in good agreement with the perovskite orthorhombic structure (PDF No. 37-1493).²⁹ For higher Sr concentration (LSFO-0.67, LSFO-0.8), the structure changes from orthorhombic to cubic. Table 1 and Fig. 1b summarize the lattice parameters and Fe-O bond lengths obtained by Rietveld refinement. The lattice parameters decrease as the Sr concentration increases, which can be associated to the formation of Fe⁴⁺ with smaller ionic radius and a shorter Fe-O bond length.³⁰ However, we found it was difficult to synthesize stoichiometric SrFeO_3 (SFO), because of its tendency to form oxygen vacancies similar to other materials such as $\text{SrCrO}_{3-\delta}$ and $\text{SrCoO}_{3-\delta}$.^{31, 32} According to iodometric titration results (See Table 1), the oxygen contents for $x < 0.67$ are nearly stoichiometric (2.996). At higher Sr level, oxygen vacancies start to form, *i.e.*, the oxygen content is ~ 2.94 for $x=0.67$ and $x=0.80$. The oxygen content for $\text{SrFeO}_{3-\delta}$ is 2.89.

The Fe oxidation state was examined by XAS at Fe *L* edges, shown in Fig. 1d. The Fe *L* edge splits into L_3 and L_2 due to spin orbit coupling and further splits into t_{2g} and e_g due to the atomic multiplet effect.³³ The Fe $L_{2,3}$ spectrum for LFO is consistent with +3 oxidation state of Fe with a d^5 high spin configuration (Fig. 1c), *i.e.*, $t_{2g}^3e_g^2$.³⁴ As x increases, the line-shape of the Fe *L* edges systematically changes due to the oxidation of Fe^{3+} to Fe^{4+} . The Fe $L_{2,3}$ spectrum for LSFO-0.8 closely resemble that of $\text{La}_{1-x}\text{Sr}_x\text{Fe}_{0.75}\text{Ni}_{0.25}\text{O}_3$ ($x = 0.75$) and BaFeO_3 , where Fe^{4+} is in a high spin state with a $t_{2g}^3e_g^1$ configuration.^{35, 36}

Nitrogen physisorption with Brunauer-Emmett-Teller (BET) method shows that all the LSFO samples have surface areas in the range of 4.1 to 6.7 $\text{m}^2 \text{ g}^{-1}$ (Fig. S2). Consistent with the small variation in the BET surface areas, the samples also exhibit very similar morphology as determined by scanning electron microscopy (Fig. S3). From these results, we can conclude that differences in OER performance are not due to a large variation in the surface areas of LSFO.

Electrochemical performance

The OER activities of the LSFO- x series and LaNiO_3 (LNO) as a benchmark sample were examined in an O_2 -saturated 1 M KOH solution using a rotating disk electrode. In order to correct for the small differences in surface area, the current densities in linear sweep voltammetry (LSV) curves were normalized to the BET surface area. Fig. 2a shows the normalized LSV after three cycles of cyclic voltammetry (CV) measurements. Fig. 2b shows the overpotential to achieve a current density of 50 $\mu\text{A cm}^{-2}_{\text{oxide}}$ and Tafel slope. It clearly shows that the specific OER activities of LSFO are significantly enhanced with increasing Sr doping. The LSFO-0.8 sample exhibits the lowest overpotential of 318 mV to achieve 50 $\mu\text{A cm}^{-2}_{\text{oxide}}$, even lower than that of the well-known highly active LNO (343 mV).^{37, 38} As further shown in Fig. 2b, the Tafel slope is reduced from 83 mV dec⁻¹ for LFO to 58 mV dec⁻¹ for LSFO-0.8. The substantial decrease of Tafel slope points to faster reaction kinetics and may imply a change of the RDS. As will be discussed in the following sections, the reduction in Tafel slope is related to the favorable adsorption of the *OH intermediate as a result of electronic modulation associated with the presence of Fe^{4+} . However, for SFO, the OER activity dramatically decreases after three cycles of measurement. This is likely due to poor stability of the tetragonal phase of $\text{SrFeO}_{3-\delta}$. Han *et al.* reported that the crystalline

structure of $\text{SrFeO}_{3-\delta}$ easily transforms into an OER inactive amorphous layer of Fe hydroxide/oxyhydroxide during OER process.³⁹

Electrochemical impedance spectroscopy (EIS) measurements were performed to investigate the kinetics of charge transfer at the electrode/electrolyte interface. Fig. 2c shows the Nyquist plots at 1.63 V vs. RHE, fitted using equivalent circuit composed of electrolyte resistance (R_s), a constant phase element (CPE) and a charge transfer resistance (R_{ct}). The fitted R_{ct} values (Table S2) decrease from 4320 Ω for LFO to 390 Ω for LSFO-0.8, suggesting enhanced interfacial charge transfer kinetics with Sr doping. In addition, we also performed OER stability tests for both LFO and LSFO-0.8, showing that both LFO and LSFO-0.8 exhibit good durability for 24 hours (Fig. 2d). We performed high resolution transmission electron microscopy (HRTEM) measurements to track the structural change for the LSFO-0.8 sample after 5 and 30 cycles CV measurements, as shown in Fig. 2e. The inner of catalyst remains its original crystalline structure after 5 and 30 cycles of CV measurements. A thin amorphous surface layer of 1-2 nm thick at some region is observed after 30 cycles of measurements. Since our specific OER activities and Tafel slopes discussed above were acquired after three cycles of measurement, these data reflect the intrinsic properties of crystalline LSFO. Taken together, all the above results confirm that while LFO is not active for OER, Sr doping significantly enhances the intrinsic activity by modulating the electronic structure.

Electronic structure

We used XPS, XAS and DFT+U calculations to examine the change of electronic structure with different Sr doping levels.⁴⁰ Fig. 3a and 3b show the VB XPS spectra and O K-edge XAS, respectively. The VB XPS measures the occupied density of states (DOS) weighted by the cross-sections of the contributing orbitals. On the other hand, O K-edge XAS measures the transition from the O 1s core level to the unoccupied DOS of hybridized O 2p and Fe 3d character. The combination of XPS VB and O K-edge XAS can be used to directly examine the electronic structure near the E_F . The VB spectrum for LFO basically consists of Fe 3d–O 2p hybridized states. According to the

experimental and calculational results reported by Wadati *et. al.* and Wang *et. al.*, the region marked as “A” close to the E_F arises mostly from two electron occupied Fe $3d_{e_g}$ orbitals, and the broad 3-9 eV region marked as “B” has more O $2p$ and Fe $3d_{t_{2g}}$ character.^{40, 41} Upon increasing Sr doping, the occupied VB DOS gradually shifts towards lower binding energy (BE), due to the hole doping effect in semiconductors, *i.e.* a p-type doping.^{42, 43} Fig. 3c summarizes the shift values of the valence band maximum (VBM) position towards the E_F as Sr doping, together with a systematic increase of the electrical conductivity as hole doping increases. As will discussed below, the shift of occupied VB to E_F optimizes the band alignment with H_2O for boosting OER.

For the O K -edge spectra (Fig. 3b), the two features “C” and “D” are attributed to unoccupied Fe $3d_{t_{2g}}$ and e_g orbitals, respectively.⁴¹ Additionally, a new unoccupied state at 528 eV (denoted as “H”) gradually increases as the Sr concentration increases. This is a direct observation of the hole state induced by the La substitution with Sr, which can be associated with the oxidation of Fe^{3+} with $t_{2g}^3e_g^2$ configuration to Fe^{4+} with a $t_{2g}^3e_g^1$ electronic configuration. The hole state dominates the unoccupied DOS when $x \geq 0.67$. From O- K edge XAS for LFO and LSFO-0.1, we can estimate that the hole state center is located ~ 0.9 eV below the bottom of conduction band of LFO. In other word, because the bandgap of LFO is 2.2 eV, the hole center is located at 1.3 eV above the VBM of LFO.

DFT+U ($U = 3$ eV) calculations were used to examine the electronic structures of LSFO. As shown in Fig. 3d, the calculated projected DOS agrees well with experimentally determined DOS by VB XPS and O- K edge XAS. La substitution with Sr creates unoccupied hole state of strongly hybridized states of Fe $3d$ and O $2p$. The overlapping of $2p$ partial DOS and Fe $3d$ partial DOS at both the occupied and unoccupied states increase as Sr content increases, because of enhanced Fe $3d$ -O $2p$ hybridization by higher Fe^{4+} oxidation state. This is consistent with the shorten Fe-O bond length in presence of Fe^{4+} as determined by XRD refinement. We also quantitatively determine the degree of Fe $3d$ -O $2p$ hybridization from O K -edge XAS based on the method developed by Suntivich *et al.*⁴⁴ (see Fig. S4 and Table S3 for details) Fig. 3e plots the degree of hybridization as a function of Sr doping level, showing that the Fe $3d$ -O $2p$ hybridization systematically increases with Sr contents.

As will be discussed in the next section, the enhanced Fe 3d-O 2p hybridization strongly correlates with the improved OER activity.

Electronic structure-OER activity

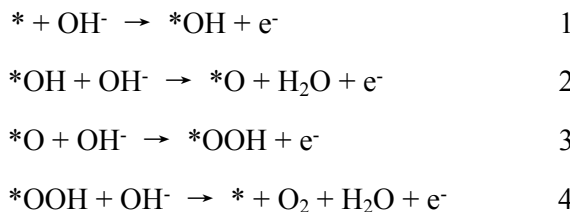
The electronic structures provide insight into rationalizing the substantial enhancement of the OER activity by Sr doping. The occupied and unoccupied DOS near the E_F determine the adsorption interaction of reaction intermediates with the LSFO surfaces. Recent studies suggested that the O 2p-band center relative to the E_F can be used as a descriptor for OER activity, in a way similar to the d-band center model for noble metal catalysts.^{45, 46} As determined by the VB spectra, Sr doping leads to gradual shift of the occupied VB, *i.e.* O p-band center, towards the E_F . Fig. 4a (left panel) plots the schematic energy band positions for LFO and LSFO-0.8, *i.e.*, conduction band minimum (CBM), and the redox potential of O_2/OH^- in a common energy scale with reference to the vacuum level. This energy diagram is constructed considering the bandgap and ionization potential of LFO are 2.2 eV and 5.7 eV respectively. This energy diagram is constructed considering the bandgap of LFO is 2.2 eV and ionization potential of LFO are 5.7 eV relative to the vacuum level. Therefore, the CBM relative to vacuum level is -3.5 eV. ($E_{CBM} = E_{\text{ionization potential}} - E_{\text{bandgap}}$).²⁰ The energy level of hole state determined by the energy difference (0.9 eV) between CBM and hole state in O K-edge XAS. Conversions between scales were performed using equations^{47, 48}:

$$E \text{ (vs. vacuum)} = [E \text{ (vs. RHE, pH = 14)} + 4.44 - 0.059 \cdot \text{pH}] \text{ eV.}$$

From this equation, the potential level verse vacuum of water oxidation is determined to be 4.84 eV. It can be seen that the shift of the energy position of the VB closer to that of absorbed oxygen intermediates leads to more effective orbital overlap. This will decrease the energetic cost to accept/donate electrons at the intermediate-catalyst interface, and therefore increase the rate of reaction.⁴⁹⁻⁵¹ As can be seen in Fig. 4b, the specific OER activities of the LSFO correlates strongly with the experimentally measured shift VBM. Moreover, our results indicate the higher Fe⁴⁺ oxidation states induce shorter Fe-O bond length and a higher degree of Fe 3d-O 2p hybridization. An increased *p-d* hybridization implies a reduced energy difference between Fe 3d and O 2p orbitals, which promotes a fast electron transfer between the Fe cations in contact with absorbed oxygen intermediates for enhanced OER activity. Fig. 4c shows the OER activity closely correlates with the degree of Fe 3d-O 2p hybridization, demonstrating a reduced transfer energy and faster electron transfer.

The hole state introduced by Sr doping also plays an important role in the kinetics of electron transfer at the solid/water interface. The energy difference between the electron-accepting state (*i.e.*, the CBM for LFO and the hole state for LSFO) and the redox potential is defined as the energy barrier (or called Schottky barrier in semiconductor physics terms) for electron transfer associated with water oxidation. This is one of the major differences between electrocatalysts based on noble metals and TM oxide semiconductors, as the former do not have a bandgap. Hong *et al.* proposed that, for TM oxides with a large charge transfer barrier, the conventional four concerted proton-electron transfer mechanism for OER is prohibited, because the electron transfer step is limited by the large Schottky barriers.⁵² This is consistent with the large electron transfer resistance measured by EIS (4320 Ω) and a high Tafel slope (83 mV dec⁻¹) for LFO. This large Schottky barrier is significantly reduced by the newly created hole states that is located at 0.9 eV below CBM. The intensity and bandwidth of the hole state increase with the Sr concentration, which results in much smaller electron transfer resistance (390 Ω in EIS) and a Tafel slope of 58 mV dec⁻¹ for the highest doping level, LSFO-0.8. This transforms the OER mechanism to concerted proton-electron transfer.

The OER process can be described in the following four elementary steps (shown in Fig. 4a, right panel).



where * represents the surface active sites and *OH, *O and *OOH represent various adsorbed reaction intermediates. According to the OER mechanistic studies using DFT calculations and molecular orbital theory by Tripkovic *et al.*⁵³, the formation of adsorbed *OH is the RDS of LFO for the OER. They also found that the absorption of reaction intermediate on the LFO surface is too weak because of the half occupied e_g orbital. Similarly, we recently found that NiO has a low OER activity, due to the weak binding of *OH intermediate on NiO surface; however, Ni³⁺ states induced by Li doping help to stabilize the adsorption of *OH, thereby improving the kinetics for OER.¹⁴ We argue that the Fe⁴⁺ states introduced by Sr doping have a similar stabilizing effect which

promotes the adsorption of *OH intermediate for fast OER. To verify this, we performed near ambient pressure XPS (NAP-XPS) measurements in the presence of 1 mbar water pressure for LSFO thin films grown on Nb doped SrTiO₃ substrates (Fig. S5a). The LSFO thin films exhibit similar electronic structures and OER activity trends as found for LSFO polycrystalline powder (Fig. S5b, c, d). Fig. 5a shows the O 1s core level spectra for the LSFO-x ($x=0$, 0.33, 0.67 and 0.8). According to previous reports for water absorption on oxide surfaces,⁵⁴⁻⁵⁶ the O 1s spectra can be fitted with four components located at 528.6 eV assigned to lattice oxygen (Ox),⁵⁷ 530.8 eV assigned to surface absorbed OH (OH), 532.7 eV assigned to surface carbonate (C-O) and 535 eV assigned to vapor phase water (H₂O_{vap}). The proportion of the OH peak at ~530.8 eV is substantially increased as the Sr concentration increases, indicating an enhanced OH adsorption capacity. This result is in agreement with recent NAP-XPS results by Stoerzinger *et al.* that 20% Sr doping in LaFeO₃ promotes the formation of surface hydroxyls.⁵⁷ Fig. 5b plots the activities as a function of the ratio of adsorbed OH relative to the lattice oxygen (Ox) for different Sr doping levels. The enhanced binding with OH may lead to a change of the RDS from OH adsorption to other steps.⁵² Recently, using *operando* Mössbauer spectroscopy, Chen *et al.* observed the formation of Fe⁴⁺ oxidation state in Fe-doped NiOOH catalysts during water oxidation.⁵⁸ A mechanistic study also suggests that the Fe⁴⁺ states serve as active sites for catalyzing the formation of active O radicals for a fast OER.⁵⁹ Both our result and literature underpin the important role of Fe⁴⁺ states for catalyzing OER in Fe-based oxides.

Conclusions

We studied in detail the correlation between the electronic structure of La_{1-x}Sr_xFeO₃ and OER performance. Replacing La with Sr substantially enhances the OER activity; La_{0.2}Sr_{0.8}FeO₃ was identified as the most active catalyst. Our spectroscopic data show that the increased OER performance can be linked to the presence of Fe^{4+:} (i) a decrease of Fe-O bond length and a concomitant increase in Fe 3d and O 2p hybridization (strong Fe-O bonds); (ii) an shift of the occupied VB, *i.e.* the Fe 3d-O 2p band to E_F, and (iii) the creation of a new hole (unoccupied) state at ~0.9 eV below the bottom of CB. The shift of the VB center and the stronger Fe 3d-O 2p hybridization help to stabilize the surface adsorption of the hydroxyl reaction intermediate which is considered as the

RDS for the OER. The emerging hole state reduces the energy barrier for electron transfer at the interface, and therefore facilitates the charge transfer rate leading to faster OER. Our study highlights the importance of in-depth understanding of the electronic structure of transition metal oxides for rational materials engineering needed to design highly active, earth-abundant metal based OER catalysts.

Experimental Section

Material synthesis. LSFO-x ($x = 0, 0.1, 0.33, 0.67, 0.8$ and 1) polycrystalline powders were synthesized by a modified Pechini sol-gel method. Stoichiometric amounts of $\text{La}(\text{NO}_3)_3$ (Alfa, 99.9%), $\text{Sr}(\text{NO}_3)_2$ (Alfa, 99.9%), and $\text{Fe}(\text{NO}_3)_3 \cdot 9\text{H}_2\text{O}$ (Alfa, 99.9%) were mixed in Milli-Q water ($18 \text{ M}\Omega \text{ cm}$). Citric acid was added as chelating agent in sequence in a 2:1 molar ratio with respect to the total metal cations. 1.2 mL of ethylene glycol was also added to the solution. After evaporation of water, the resultant gel was heated in furnace at 350°C for 2 hours in air to form a brown precursor. The precursor was grounded and calcined at 900°C for 6 hours in 1 atm O_2 gas. LaNiO_3 was also prepared by this method except that nickel nitrate was used instead of iron nitrate. The LSFO thin films used for NAP-XPS measurements were grown on (001) oriented Nb-doped SrTiO_3 substrates by pulsed laser deposition from respective targets. Laser ablation was performed at a repetition rate of 5 Hz and an energy density of 1.5 J/cm^2 with a 248 nm KrF excimer laser. Films with thicknesses of 30 nm were grown at a substrate temperature of 700°C in oxygen partial pressures 100 mTorr. The crystal structure and epitaxial relationship in the films was confirmed by high-resolution XRD using PANalytical four-circle diffractometer in θ - 2θ scans.

Physicochemical Characterization. The samples were characterized by XRD (Rigaku, Japan) with $\text{Cu } K\alpha$ radiation ($\lambda = 0.15418 \text{ nm}$) operating at 40 kV and 40 mA emission current. Rietveld refinement was used to determine lattice parameters and the crystal structure by GSAS software and EXPGUI interface. The metal concentration of $\text{La}_{1-x}\text{Sr}_x\text{FeO}_3$ was measured by conducting inductively coupled plasma optical emission spectroscopy (ICP-OES) measurements. Sample morphology and nano/microstructure were examined by scanning electron microscopy (ZEISS, Germany) and Tecnai F-30

transmission electron microscopy (FEI, USA). The samples were dispersed in a solution of water/isopropanol with volume ratio of 3:1 by ultrasonication for 30 minutes to form a homogeneous ink and then dropped on a silicon slice for SEM and Cu grid for HRTEM. In order to exclude the interference of Nafion on HRTEM for the sample after OER, Nafion solution was not added in the ink when preparing the work electrode for HRTEM characterization. The Brunauer-Emitter-Teller (BET) specific surface area was obtained by the isothermal N_2 adsorption and desorption at 77 K (ASAP 2020, Micromeritics, USA). Electrical conductivity was measured using a Keithley 2401 Source Meter at room temperature. Oxygen non-stoichiometry was determined by iodometry titration method. For XPS and XAS measurements, the powders were pressed into pellets. XPS were measured using a monochromatic Al $K\alpha_1$ x-ray ($h\nu = 1486.6$ eV) source at normal emission (electron take-off angle = 90° relative to the surface plane) with a SPECS PHOIBOS 150 electron energy analyzer. The total energy resolution was about 0.50 eV. The binding energy (BE) was calibrated using a polycrystalline Au foil placed in electrical contact with the samples. VB spectra for LSFO was measured in the binding energy range of 0-10 eV. XAS measurements were performed at the Soft X-ray Spectroscopy Beamline of the Australian Synchrotron. The XAS measurements at the O K -edge and Fe L edge were performed in total electron yield (TEY) using linearly polarized X-rays. Near-ambient pressure XPS were recorded on a lab-based spectrometer (SPECS GmbH, Berlin) using a monochromated Al $K\alpha$ source ($h\nu = 1486.6$ eV) operating at 30 W. The X-rays are microfocused to give a spot size on the thin films of 300 μm in diameter. The analyser is a SPECS PHOIBOS 150 NAP, a 180° hemispherical energy analyser with 150 mm mean radius. The entrance to the analyser is a nozzle with a 300 μm diameter orifice. The total energy resolution of the measurements was about 0.50 eV. The BE was calibrated against the Au Fermi level. Prior water vapor exposure, samples were annealed to 400 °C in 1 mbar O_2 for cleaning purpose.

Electrochemical measurements. The electrochemical measurements were performed on a three-electrode system controlled by an electrochemical workstation (CHI 760E) connected with glassy carbon rotating disk electrode configuration (Pine Research Instrumentation). For OER tests, an Hg/HgO (1 M KOH) electrode was used as the reference electrode, and a graphite rod was used as the counter electrode. All tests were performed in O_2 -saturated 1 M KOH (Adamas, 99.999%) electrolyte (pH =

14) using a catalyst-modified glassy carbon (GC) working electrode (0.196 cm^2). To prepare the working electrodes, $10\text{ }\mu\text{L}$ catalyst ink were prepared by dispersing 5 mg LSFO powder in 1 mL of $750\text{ }\mu\text{L H}_2\text{O}$ and $250\text{ }\mu\text{L}$ isopropanol and $50\text{ }\mu\text{L}$ 5 wt% Nafion solution. The ink was ultrasonicated for 30 minutes and then drop-cast on the GC surface with a catalyst loading of $0.25\text{ mg cm}^{-2}\text{ oxide}$. Cyclic voltammetry tests were performed at a scan rate of 0.1 V s^{-1} and a rotation of 1600 rpm from 0.2 V to 0.8 V vs. Hg/HgO . LSV data were collected at 10 mV s^{-1} . Ohmic losses were corrected by i-R test from the potentiostat. The Tafel slope was extracted from LSV data. The electrochemical impedance spectroscopy (EIS) measurements were performed at 0.73 V (vs. Hg/HgO) under an alternating voltage of 5 mV from 100 kHz to 0.1 Hz . All potential values were calibrated to reversible hydrogen electrode (RHE) using the following equation: $E(\text{RHE}) = 0.0591 \times \text{pH} + E_{\text{Hg/HgO}} + E_{\text{applied}}$. Electrochemical stability test was performed in chronopotentiometry mode.

Author contributions

Z.C.S prepared the samples and carried out electrochemical measurements with the help of X.C.H and M.Y.C. Y.B.Z and J.C did the theoretical DOS calculation. F.E.O performed the near ambient pressure XPS. A.T, D.C.Q and K.H.L.Z performed and XAS at Australian Synchrotron. W.W.L performed photoemissions spectroscopy. K.H.L.Z directed the project. All authors were involved in discussion and writing the manuscript.

Conflicts of interest

There are no conflicts of interest to declare.

ACKNOWLEDGMENTS

K.H.L. Zhang is grateful for funding support by National Natural Science Foundation of China (Grant No. 21872116). D. Q. acknowledges the support of the Australian Research Council (Grant No. FT160100207). J.C. gratefully acknowledge the financial support by the National Natural Science Foundation of China (Grant No. 21621091 and Grant No. 21373166). We also thank beamline scientist Dr. Bruce Cowie at Australian Synchrotron for his kind assistance. Part of this research was undertaken on the Soft X-ray Spectroscopy beamline at the Australian Synchrotron, part of ANSTO. F.E.O., J.P.H. and E.J.M.H. acknowledge funding from the

Netherlands Organization for Scientific Research NWO via the gravitation program
MCEC – Netherlands Center for Multiscale Catalytic Energy Conversion.

Reference

1. P. P. Edwards, V. L. Kuznetsov, W. I. F. David and N. P. Brandon, *Energy Policy*, 2008, **36**, 4356-4362.
2. I. C. Man, H.-Y. Su, F. Calle-Vallejo, H. A. Hansen, J. I. Martínez, N. G. Inoglu, J. Kitchin, T. F. Jaramillo, J. K. Nørskov and J. Rossmeisl, *ChemCatChem*, 2011, **3**, 1159-1165.
3. S. Park, Y. Shao, J. Liu and Y. Wang, *Energy Environ. Sci.*, 2012, **5**, 9331-9344.
4. J. Hwang, R. R. Rao, L. Giordano, Y. Katayama, Y. Yu and Y. Shaohorn, *Science*, 2017, **358**, 751-756.
5. A. Grimaud, A. Demortière, M. Saubanère, W. Dachraoui, M. Duchamp, M.-L. Doublet and J.-M. Tarascon, *Nature Energy*, 2016, **2**, 16189.
6. Y. Matsumoto and E. Sato, *Mater. Chem. Phys.*, 1986, **14**, 397-426.
7. J. O. M. Bockris and T. Otagawa, *J. Phys. Chem.*, 1983, **87**, 2960-2971.
8. X. Cheng, E. Fabbri, M. Nachtegaal, I. E. Castelli, M. El Kazzi, R. Haumont, N. Marzari and T. J. Schmidt, *Chem. Mater.*, 2015, **27**, 7662-7672.
9. J. Suntivich, K. J. May, H. A. Gasteiger, J. B. Goodenough and Y. Shao-Horn, *Science*, 2011, **334**, 1383-1385.
10. A. Grimaud, K. J. May, C. E. Carlton, Y.-L. Lee, M. Risch, W. T. Hong, J. Zhou and Y. Shao-Horn, *Nat. Commun.*, 2013, **4**, 2439.
11. S. Yagi, I. Yamada, H. Tsukasaki, A. Seno, M. Murakami, H. Fujii, H. Chen, N. Umezawa, H. Abe, N. Nishiyama and S. Mori, *Nat. Commun.*, 2015, **6**, 8249.
12. A. Grimaud, O. Diaz-Morales, B. Han, W. T. Hong, Y.-L. Lee, L. Giordano, K. A. Stoerzinger, M. T. M. Koper and Y. Shao-Horn, *Nat. Chem.*, 2017, **9**, 457.
13. B. Hua, M. Li, W. Pang, W. Tang, S. Zhao, Z. Jin, Y. Zeng, B. Shalchi Amirkhiz and J.-L. Luo, *Chem*, 2018, **4**, 2902-2916.
14. G. Fu, X. Wen, S. Xi, Z. Chen, W. Li, J.-Y. Zhang, A. Tadich, R. Wu, D.-C. Qi, Y. Du, J. Cheng and K. H. L. Zhang, *Chem. Mater.*, 2019, **31**, 419-428.
15. L. Wang, K. A. Stoerzinger, L. Chang, X. Yin, Y. Li, C. S. Tang, E. Jia, M. E. Bowden, Z. Yang, A. Abdelsamie, L. You, R. Guo, J. Chen, A. Rusydi, J. Wang, S. A. Chambers and Y. Du, *ACS Appl. Mater. Interfaces*, 2019, **11**, 12941-12947.
16. Z. Xia and S. Guo, *Chem. Soc. Rev.*, 2019, **48**, 3265-3278.
17. Y. Yao, S. Hu, W. Chen, Z.-Q. Huang, W. Wei, T. Yao, R. Liu, K. Zang, X. Wang, G. Wu, W. Yuan, T. Yuan, B. Zhu, W. Liu, Z. Li, D. He, Z. Xue, Y. Wang, X. Zheng, J. Dong, C.-R. Chang, Y. Chen, X. Hong, J. Luo, S. Wei, W.-X. Li, P. Strasser, Y. Wu and Y. Li, *Nat. Catal.*, 2019, **2**, 304-313.
18. H. A. Tahini, X. Tan, U. Schwingenschlögl and S. C. Smith, *ACS Catal.*, 2016, **6**, 5565-5570.
19. J. T. Mefford, X. Rong, A. M. Abakumov, W. G. Hardin, S. Dai, A. M. Kolpak, K. P. Johnston and K. J. Stevenson, *Nat. Commun.*, 2016, **7**, 11053.
20. M. D. Scafetta, A. M. Cordi, J. M. Rondinelli and S. J. May, *J. Phys.: Condens. Matter*, 2014, **26**, 505502.
21. K. J. May, D. P. Fenning, T. Ming, W. T. Hong, D. Lee, K. A. Stoerzinger, M. D. Biegalski, A. M. Kolpak and Y. Shao-Horn, *J. Phys. Chem. Lett.*, 2015, **6**, 977-985.

22. J.-J. Xu, Z.-L. Wang, D. Xu, F.-Z. Meng and X.-B. Zhang, *Energy Environ. Sci.*, 2014, **7**, 2213-2219.
23. Z. Dai, C.-S. Lee, B.-Y. Kim, C.-H. Kwak, J.-W. Yoon, H.-M. Jeong and J.-H. Lee, *ACS Appl. Mater. Interfaces*, 2014, **6**, 16217-16226.
24. F. H. Taylor, J. Buckeridge and C. R. A. Catlow, *Chem. Mater.*, 2016, **28**, 8210-8220.
25. Y. Zhu, W. Zhou, J. Yu, Y. Chen, M. Liu and Z. Shao, *Chem. Mater.*, 2016, **28**, 1691-1697.
26. A. Wattiaux, J. C. Grenier, M. Pouchard and P. Hagenmuller, *J. Electrochem. Soc.*, 1987, **134**, 1714-1718.
27. S. She, J. Yu, W. Tang, Y. Zhu, Y. Chen, J. Sunarso, W. Zhou and Z. Shao, *ACS Appl. Mater. Interfaces*, 2018, **10**, 11715-11721.
28. A. E. Danks, S. R. Hall and Z. Schnepf, *Materials Horizons*, 2016, **3**, 91-112.
29. T. Peterlin-Neumaier and E. Steichele, *J. Magn. Magn. Mater.*, 1986, **59**, 351-356.
30. S. Erat, A. Braun, C. Piamonteze, Z. Liu, A. Ovalle, H. Schindler, T. Graule and L. J. Gauckler, *J. Appl. Phys.*, 2010, **108**, 124906.
31. A. M. Arévalo-López, J. A. Rodgers, M. S. Senn, F. Sher, J. Farnham, W. Gibbs and J. P. Attfield, *Angew. Chem. Int. Ed.*, 2012, **51**, 10791-10794.
32. H. Jeen, W. S. Choi, J. W. Freeland, H. Ohta, C. U. Jung and H. N. Lee, *Adv. Mater.*, 2013, **25**, 3651-3656.
33. M. L. Baker, M. W. Mara, J. J. Yan, K. O. Hodgson, B. Hedman and E. I. Solomon, *Coord. Chem. Rev.*, 2017, **345**, 182-208.
34. S. Jana, S. K. Panda, D. Phuyal, B. Pal, S. Mukherjee, A. Dutta, P. A. Kumar, D. Hedlund, J. Schött, P. Thunström, Y. Kvashnin, H. Rensmo, M. V. Kamalakar, C. U. Segre, P. Svedlindh, K. Gunnarsson, S. Biermann, O. Eriksson, O. Karis and D. D. Sarma, *Phys. Rev. B*, 2019, **99**, 075106.
35. S. Erat, A. Braun, A. Ovalle, C. Piamonteze, Z. Liu, T. Graule and L. J. Gauckler, *Appl. Phys. Lett.*, 2009, **95**, 174108.
36. T. Tsuyama, T. Matsuda, S. Chakraverty, J. Okamoto, E. Ikenaga, A. Tanaka, T. Mizokawa, H. Y. Hwang, Y. Tokura and H. Wadati, *Phys. Rev. B*, 2015, **91**, 115101.
37. W. T. Hong, M. Risch, K. A. Stoerzinger, A. Grimaud, J. Suntivich and Y. Shao-Horn, *Energy Environ. Sci.*, 2015, **8**, 1404-1427.
38. J. R. Petrie, V. R. Cooper, J. W. Freeland, T. L. Meyer, Z. Zhang, D. A. Lutterman and H. N. Lee, *J. Am. Chem. Soc.*, 2016, **138**, 2488-2491.
39. B. Han, A. Grimaud, L. Giordano, W. T. Hong, O. Diaz-Morales, L. Yueh-Lin, J. Hwang, N. Charles, K. A. Stoerzinger, W. Yang, M. T. M. Koper and Y. Shao-Horn, *J. Phys. Chem. C*, 2018, **122**, 8445-8454.
40. L. Wang, Y. Du, P. V. Sushko, M. E. Bowden, K. A. Stoerzinger, S. M. Heald, M. D. Scafetta, T. C. Kaspar and S. A. Chambers, *Phys. Rev. Materials*, 2019, **3**, 025401.
41. H. Wadati, D. Kobayashi, H. Kumigashira, K. Okazaki, T. Mizokawa, A. Fujimori, K. Horiba, M. Oshima, N. Hamada, M. Lippmaa, M. Kawasaki and H. Koinuma, *Phys. Rev. B*, 2005, **71**, 035108.
42. K. H. L. Zhang, Y. Du, A. Papadogianni, O. Bierwagen, S. Sallis, L. F. J. Piper, M. E. Bowden, V. Shutthanandan, P. V. Sushko and S. A. Chambers, *Adv. Mater.*, 2015,

- 27, 5191-5195.
43. J. Y. Zhang, W. W. Li, R. L. Z. Hoye, J. L. MacManus-Driscoll, M. Budde, O. Bierwagen, L. Wang, Y. Du, M. J. Wahila, L. F. J. Piper, T. L. Lee, H. J. Edwards, V. R. Dhanak and K. H. L. Zhang, *Journal of Materials Chemistry C*, 2018, **6**, 2275-2282.
 44. J. Suntivich, W. T. Hong, Y.-L. Lee, J. M. Rondinelli, W. Yang, J. B. Goodenough, B. Dabrowski, J. W. Freeland and Y. Shao-Horn, *J. Phys. Chem. C*, 2014, **118**, 1856-1863.
 45. J. K. Nørskov, F. Abild-Pedersen, F. Studt and T. Bligaard, *Proc. Natl. Acad. Sci.*, 2011, **108**, 937.
 46. W. Yang, Z. Wang, W. Zhang and S. Guo, *Trends in Chemistry*, 2019, **1**, 259-271.
 47. S. Trasatti, *Pure Appl. Chem.*, 1986, **58**, 955-966.
 48. D. A. Kuznetsov, B. Han, Y. Yu, R. R. Rao, J. Hwang, Y. Román-Leshkov and Y. Shao-Horn, *Joule*, 2018, **2**, 225-244.
 49. B. B. Smith, J. W. Halley and A. J. Nozik, *Chem. Phys.*, 1996, **205**, 245-267.
 50. R. A. Marcus, *J. Chem. Phys.*, 1965, **43**, 3477-3489.
 51. H. Gerischer, *J. Phys. Chem.*, 1991, **95**, 1356-1359.
 52. W. T. Hong, K. A. Stoerzinger, Y.-L. Lee, L. Giordano, A. Grimaud, A. M. Johnson, J. Hwang, E. J. Crumlin, W. Yang and Y. Shao-Horn, *Energy Environ. Sci.*, 2017, **10**, 2190-2200.
 53. V. Tripkovic, H. A. Hansen, IJ. M. Garcia-Lastra and T. Vegge, *J. Phys. Chem. C*, 2018, **122**, 1135-1147.
 54. K. A. Stoerzinger, X. Renshaw Wang, J. Hwang, R. R. Rao, W. T. Hong, C. M. Rouleau, D. Lee, Y. Yu, E. J. Crumlin and Y. Shao-Horn, *Top. Catal.*, 2018, **61**, 2161-2174.
 55. K. A. Stoerzinger, Y. Du, K. Ihm, K. H. L. Zhang, J. Cai, J. T. Diulus, R. T. Frederick, G. S. Herman, E. J. Crumlin and S. A. Chambers, *Advanced Materials Interfaces*, 2018, **5**, 1701363.
 56. K. A. Stoerzinger, W. T. Hong, E. J. Crumlin, H. Bluhm and Y. Shao-Horn, *Acc. Chem. Res.*, 2015, **48**, 2976-2983.
 57. K. A. Stoerzinger, L. Wang, Y. Ye, M. Bowden, E. J. Crumlin, Y. Du and S. A. Chambers, *J. Mater. Chem. A*, 2018, **6**, 22170-22178.
 58. J. Y. C. Chen, L. Dang, H. Liang, W. Bi, J. B. Gerken, S. Jin, E. E. Alp and S. S. Stahl, *J. Am. Chem. Soc.*, 2015, **137**, 15090-15093.
 59. H. Xiao, H. Shin and W. A. Goddard, *Proc. Natl. Acad. Sci.*, 2018, **115**, 5872-5877.

Table 1. Lattice parameters and Fe-O bond lengths extracte©©d from Rietveld refined X-ray diffraction (XRD), the oxygen concentrations determined by iodometric titration method, and the BET surface areas of LSFO.

Sample	Space group	Lattice parameters(Å)	<Fe-O> Length(Å)	Oxygen contents	BET area (m ² /g)
LFO	<i>Pnma</i>	<i>a</i> =5.558, <i>b</i> =7.858, <i>c</i> =5.569	2.009	2.996±0.002	4.9
0.1	<i>Pnma</i>	<i>a</i> =5.556, <i>b</i> =7.893, <i>c</i> =5.545	1.992	2.997±0.008	6.7
0.33	<i>Pnma</i>	<i>a</i> =5.518, <i>b</i> =7.812, <i>c</i> =5.513	1.984	2.973±0.007	6.1
0.67	<i>Pm-3m</i>	<i>a</i> = <i>b</i> = <i>c</i> =3.881	1.941	2.951±0.014	4.3
0.8	<i>Pm-3m</i>	<i>a</i> = <i>b</i> = <i>c</i> =3.861	1.935	2.947±0.012	4.1
SFO	<i>I₄/mmm</i>	<i>a</i> = <i>b</i> =10.931, <i>c</i> =7.711	1.929	2.896±0.021	4.4

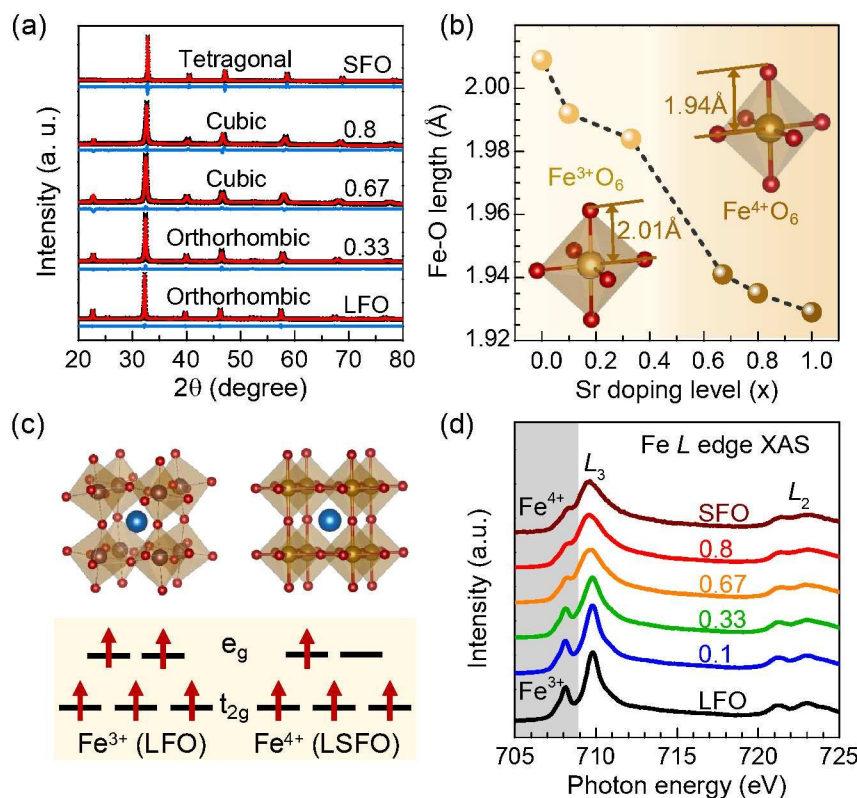


Fig. 1. (a) Rietveld refined XRD patterns for LSFO- x , $x = 0, 0.33, 0.67, 0.8$ and 1. (b) Fe-O bond lengths as a function of x obtained from Rietveld refined XRD. (c) Representative crystal structure of orthorhombic phase (LFO) and cubic phase (LSFO-0.8), and the corresponding Fe^{3+} ($3d^5$) and Fe^{4+} ($3d^4$) electron configurations in octahedral crystal field, respectively. (d) Fe $L_{2,3}$ edge XAS spectra for LSFO- x series.

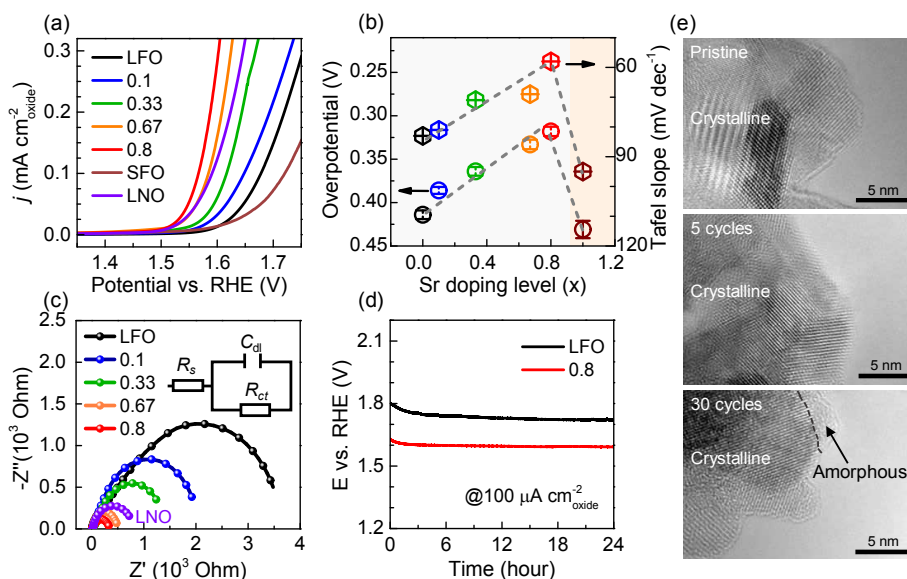


Fig. 2. (a) LSV polarization curves for LSFO- x ($x = 0, 0.1, 0.33, 0.67, 0.8$ and 1) and LNO with current density normalized by BET surface area. (b) Overpotentials to achieve 50 μ A cm $^{-2}$ and Tafel slope values as a function of Sr doping level. (c) Nyquist plots of the EIS at 1.63 V vs. RHE with a sweep frequency range of 100 kHz to 1 Hz and the equivalent circuit (inset) for fitting the data, consisting of an electrolyte resistance (R_s), a charge transfer resistance (R_{ct}) with an electrical double-layer capacitance (C_{dl}). (d) Long term stability of the LFO and LSFO-0.8 at an applied current density of 100 μ A cm $^{-2}$ oxide. (e) HRTEM images of as-synthesized LSFO-0.8 sample (top), after 5 (middle) and 30 cycles (bottom) of OER measurement, respectively.

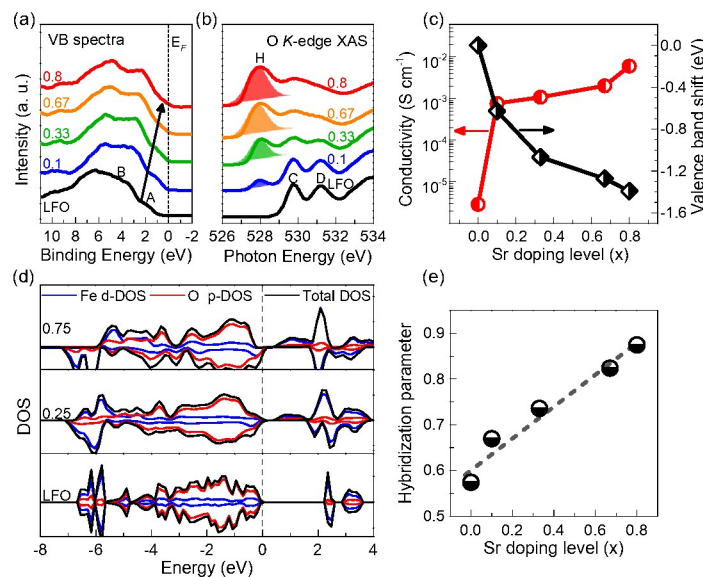


Fig. 3. (a) VB XPS spectra and (b) O K-edge XAS of LSFO- x ($x = 0, 0.1, 0.33, 0.67$ and 0.8). The VBM shows a gradual shift towards E_F . The VBM is determined by linear extrapolation of the leading edge of the VBM to zero baseline intensity. (b) The O K-edge XAS show the development of a hole state at 528 eV. (c) VBM shift values relative to LFO VBM and electrical conductivity as a function of x . (d) Density of states (DOS) calculated by DFT+U ($U = 3$ eV) for LFO, LSFO- 0.25 and LSFO- 0.75 . (e) Estimated degree of Fe 3d-O 2p hybridization as a function of Sr doping level.

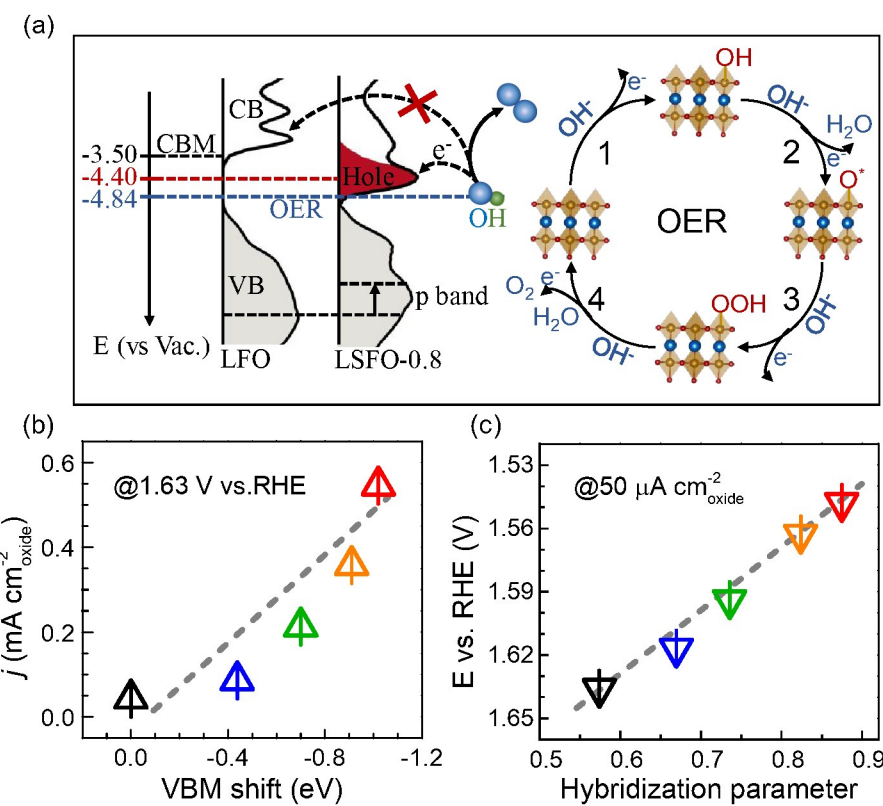


Fig. 4. (a) Left panel: experimentally measured occupied and unoccupied DOS near the E_F for LFO and LSFO-0.8; the energy level is relative to vacuum level (vs. Vac.). The redox level for O_2/H_2O (blue line) is located at -4.84 eV; the CBM level for LFO is at -3.50 eV, and the newly created hole state center for LSFO-0.8 is at -4.40 eV; the hole state effectively reduces the charge transfer barrier for OER. Right panel: schematics of the four-step reaction pathway of OER. (b) Correlation of specific OER activity (current density at 1.63 V vs. RHE) with the shift of valence band. (c) Correlation of overpotential (vs. RHE at $50 \mu\text{A cm}^{-2}_{\text{oxide}}$) with hybridization parameter.

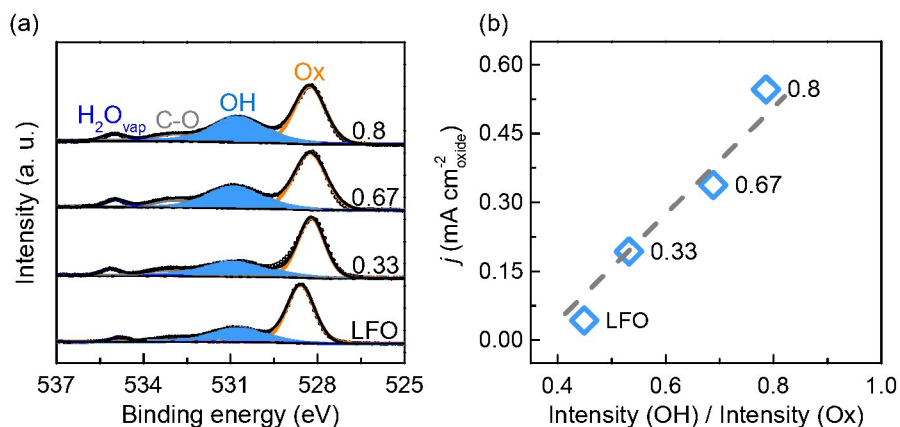
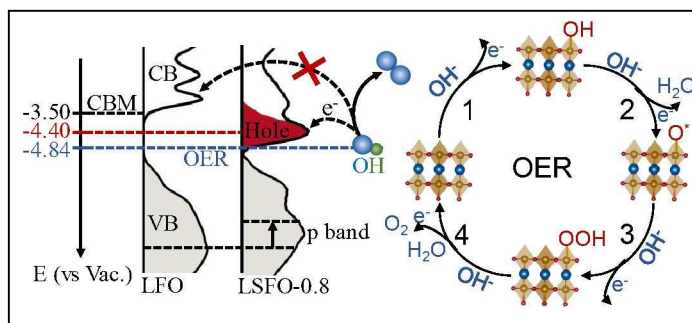


Fig. 5. (a) O 1s NAP-XPS spectra for LSFO thin films in the presence of 1 mbar H_2O vapor pressure. The O 1s spectra are fitted with four components including lattice oxygen (“Ox”, orange) at ~ 528.6 eV, surface absorbed OH (“OH”, light blue) at ~ 530.8 eV, surface carbonate (“C-O”, gray) at ~ 532.7 eV, and vapor phase H_2O (“ $\text{H}_2\text{O}_{\text{vap}}$ ”, blue) at ~ 535 eV. (b) OER current densities of LSFO thin films at 1.63 V vs. RHE vs. the ratio of adsorbed OH relative to lattice oxygen (Ox).

TOC Graphic



Hole for faster OER: The emerging hole state induced by Fe⁴⁺ plays a role to improve the OER process, *i.e.*, adsorption of OH. It reduces the energy barrier for electron transfer at the interface and facilitates a faster electron transfer from reaction intermediates to the catalyst.